Coastal Engineering 179 (2023) 104245

Contents lists available at ScienceDirect

Coastal Engineering

journal homepage: www.elsevier.com/locate/coastaleng

Fully-coupled hydroelastic modeling of a deformable wall in waves

Zhengyu Hu [a], Luofeng Huang [b], Yuzhu Li [a,*]

[a] National University of Singapore, Department of Civil and Environmental Engineering, Singapore
[b] Cranfield University, School of Water, Energy and Environment, Cranfield, UK

ARTICLE INFO

Dataset link: https://github.com/huzhengyu/wave2solids

Keywords:
Hydroelasticity
Deformable structures
Wave–structure interaction
Fully-coupled simulation
OpenFOAM

ABSTRACT

The hydroelastic behavior of a vertical wall in periodic waves is investigated using a fully-coupled computational fluid dynamics (CFD) and computational solid mechanics (CSM) model. The present numerical model is verified against previous numerical and experimental results on wave evolution and structural displacement. Then the hydrodynamic characteristics and the structural responses of an elastic wall in periodic waves are parametrically investigated. It is demonstrated that wave reflection, run-up, and loading decrease as the wall becomes more flexible. The decreases also occur when the waves become shorter. With nonlinear wave propagation, both the displacement and the stress of the wall are larger in the shoreward direction than those in the seaward direction. The wall displacement has the same frequency as the exciting waves and the stress increases with the decrease of the ratio of the wave frequency to the wall's natural frequency. Considering the effect of flexibility, empirical formulae are proposed for predicting the wave run-up, loading, and maximum displacement of the wall. Besides, the optimization of the flexible wall is conducted by taking into account both the defense performance (i.e., transmission coefficient) and the structural integrity (i.e., maximum von Mises stress). Finally, the effect of the material damping is studied, which shows that the material damping has a negligible effect on the interaction between periodic waves and the elastic structure.

1. Introduction

Sea-level rise, extreme marine events, together with increasing flood risk due to climate change put coastal communities at growing threats (Field and Barros, 2014; Ranasinghe, 2016; Toimil et al., 2020; Nicholls and Cazenave, 2010). The existing coastal and offshore structures are often designed as rigid in the majority of engineering practices. However, traditional hard structures have to suffer costly maintenance and repair, especially after extreme storm events. In many situations, they are old and poor-maintained, which increases the coastal vulnerability (Jin et al., 2015). Therefore, investigating and optimizing the characteristics of flexible structures subjected to waves can be a significant research direction.

Many studies were devoted to the interaction between waves and perfectly rigid structures (Huang et al., 2022). Reeve et al. (2008) numerically investigated the discharges of overflow and wave overtopping over a rigid seawall with various freeboard and slope conditions subjected to irregular waves. They derived empirical formulae to predict the discharges with consideration of the overflow and the wave overtopping effects. Hsiao and Lin (2010) studied solitary waves impinging on a rigid trapezoidal seawall with experimental and numerical approaches. They found that the maximum wave force often occurs with the minimum freeboard and the wave run-up to the overtopping stage, which might lead to substantial structural damage and instability. Ning et al. (2017) carried out a numerical study on the interaction between the focused wave and a vertical rigid wall through a higher-order boundary element method. They observed that wave nonlinearity can increase the wave pressure on the wall. Attili et al. (2021) numerically investigated the hydrodynamic characteristics of the landslide-tsunamis impacting dams considering the three-dimensional effects of both oblique waves and arch dams. They proposed empirical formulae for predicting the wave loading, run-up, overtopping volume, and maximum overtopping depth for dams.

However, it has been observed that steep-fronted rigid structures can induce full wave reflection, which can yield aggravated scour and impair the stability of the structure. Although it is yet to be built in practice, flexible structures showed better hydrodynamic performance and wave damping effect compared to rigid structures in the recent laboratory studies. For example, Sree et al. (2021) performed an experimental study on the evolution of periodic waves interacting with a submerged viscoelastic plate. They reported that the most flexible plate placed close to the mean water level can yield a nearly complete cutoff of wave energy transmission. Nevertheless, to date, detailed laboratory studies on the interaction between progressive waves and steep-fronted

* Corresponding author.
E-mail address: pearl.li@nus.edu.sg (Y. Li).

https://doi.org/10.1016/j.coastaleng.2022.104245
Received 1 June 2022; Received in revised form 2 October 2022; Accepted 28 October 2022
Available online 5 November 2022
0378-3839/

flexible structures are lacking. A few analytical and numerical investigations have been conducted on the hydroelastic interaction between water waves and vertical walls. For example, He and Kashiwagi (2009) simulated the vibration of a vertical rigid wall connected to a linear spring at back under the impact of a nonlinear pulse-type wave. They found that the nonlinear effect can cause an obvious discrepancy in the wall's motion compared with the linear analytical solution. Peter and Meylan (2010) analytically described the vibration of an elastic wall in linear waves based on a generalized eigenfunction expansion method. He and Kashiwagi (2012) later investigated the hydroelastic behavior of both the top-fixed and the top-free walls with a bottom-fixed end in a solitary wave based on the potential flow and the linear beam assumptions. They coupled the fluid and the solid by combining the boundary element method and the finite element model in a monolithic way (i.e., solving fluid and solid motions with a single solver). Akrish et al. (2018) simulated the elastic wall in an incident wave group by a high-order spectral method, where the linear beam model was applied. They found that the hydroelastic effect can relax or amplify both hydrodynamic characteristics (i.e., wave run-up and force) and structural oscillations. However, the linear assumptions used in the above numerical solutions for either the fluid or the solid may have limited accuracies when predicting the finite-strain structure and nonlinear wave interactions.

As such numerical simulations involve the interaction between two physical domains, i.e., the fluid and the solid, some coupling algorithms have been developed for the numerical models. Dermentzoglou et al. (2021) adopted a one-way coupling of computational fluid dynamics (CFD) and finite element method (FEM) to investigate the failure of a recurved wall with different concrete classes. Sriram and Ma (2012) simulated the interaction between the breaking wave and an elastic wall. The fluid and the solid were solved in a partitioned approach with a near-strongly coupling at the interface, i.e., fluid particles maintained their positions from the end of the previous time step during fluid–structure-interaction (FSI) iterations. Liao and Hu (2013) proposed a FDM–FEM model (where FDM stands for the finite difference method) to investigate the interaction between the surface flow and a thin elastic wall with large deformation. The standard linear beam element was employed and coupled with the fluid using a conservative momentum-exchange method based on the immersed boundary method. Kumar and Sriram (2020) simulated the breaking wave impacting on an elastic wall with a linear beam theory. They strongly coupled the fluid and the solid based on an iterative scheme. To avoid the ideal linear assumptions that have been used in most of the previous studies, Tuković et al. (2018) and Cardiff et al. (2018) developed an open-source toolbox integrating the fluid and the solid fields using the finite volume method in the OpenFOAM framework. This integrated model can be used for both fluids with nonlinear dynamics and structures with nonlinear mechanical laws (i.e., the stress tensor is a nonlinear function of the displacement vector). Huang et al. (2019) combined this model with the wave generation toolbox waves2Foam (Jacobsen et al., 2012) to investigate the hydroelastic effects of a nonlinear ice sheet in monochromatic waves. Huang and Li (2022) further improved the model to study the hydroelasticity of a submerged horizontal-plate breakwater in nonlinear waves. They observed a better wave-damping performance with a deformable plate. To the authors' knowledge, a detailed investigation of the nonlinear interaction between progressive waves and a vertical elastic wall has not been conducted yet.

The present work combines the IHFOAM wave-modeling toolbox (Higuera et al., 2013) with a fully-coupled FSI approach (Tuković et al., 2018; Cardiff et al., 2018) to study the hydroelasticity of a vertical wall in periodic waves, aiming to get an overall insight into the nonlinear wave evolution and the corresponding structural response. The paper is organized as follows. The computational approach is described in Section 2 followed by the numerical setup in Section 3. Thereafter, the FSI model is verified against the numerical results of He and Kashiwagi (2012) and validated against the experimental results of Didier et al. (2014), as in Section 4. In Section 5, simulations are conducted for an elastic cantilever wall with different bending stiffness under nonlinear wave loading. The hydrodynamic and structural behaviors are investigated and optimized. Empirical formulae are proposed for the wave run-up, loading, and wall displacement estimations. Besides, the effect of the material damping on the hydroelasticity is investigated. Section 6 provides the conclusions.

2. Numerical method

The present numerical model consists of computational fluid dynamics (CFD) and computational solid mechanics (CSM) together with a fully-coupled algorithm. The governing equations are listed as follows.

2.1. Computational fluid dynamics

The CFD model solves the Navier–Stokes equations for incompressible, isothermal, and Newtonian flows:

$$\nabla \cdot \mathbf{u} = 0 \tag{1}$$

$$\frac{\partial(\rho\mathbf{u})}{\partial t} + \nabla \cdot (\rho\mathbf{u}\mathbf{u}^T) = -\nabla p + \nabla \cdot \boldsymbol{\tau} + \rho\mathbf{g} \tag{2}$$

where $\mathbf{u}$ is the velocity vector of the water–air mixture, ρ is the density, p is the pressure, $\mathbf{g}$ is the gravitational acceleration, and $\boldsymbol{\tau}$ is viscous stress tensor defined by $\boldsymbol{\tau} = \mu\left(\nabla\mathbf{u} + \nabla\mathbf{u}^T\right)$, in which μ is the dynamic viscosity of the fluid.

The laminar flow model is employed in this simulation following Huang and Li (2022) since the turbulent effects are expected to be negligible in the present cases (i.e., no wave breaking), which can effectively reduce the computational costs. Free surface simulations utilize the IHFOAM model (Higuera et al., 2013) for wave generation and absorption. The Volume of Fluid (VOF) approach (Hirt and Nichols, 1981) is applied to capture the water–air interface with a defined phase indicator (α) denoting the proportion of the water volume in each discrete cell. α varies from 0 to 1 with $\alpha = 1$ denoting a cell full of water and $\alpha = 0$ indicating a cell full of air. Its transport equation is:

$$\frac{\partial\alpha}{\partial t} + \nabla \cdot (\mathbf{u}\alpha) + \nabla \cdot \left[\mathbf{u_c}\alpha(1-\alpha)\right] = 0 \tag{3}$$

where $\mathbf{u_c}$ is the interface compression velocity between air and water for the purpose of reducing the numerical diffusion (Weller et al., 1998). Furthermore, the mixed density and viscosity can be weighted in terms of α:

$$\rho = \alpha\rho_w + (1-\alpha)\rho_a \tag{4}$$

$$\mu = \alpha\mu_w + (1-\alpha)\mu_a \tag{5}$$

where $\rho_w = 1000\ \mathrm{kg/m^3}$ is the water density, $\rho_a = 1\ \mathrm{kg/m^3}$ is the air density, $\mu_w = 1\times10^{-3}\ \mathrm{N\ s/m^2}$ is the dynamic viscosity of the water, and $\mu_a = 1.48\times10^{-5}\ \mathrm{N\ s/m^2}$ is the dynamic viscosity of the air.

2.2. Computational solid mechanics

Considering finite strains of the solid domain, the nonlinear mechanical constitutive law, i.e., Neo-Hookean hyperelastic law, as implemented in Cardiff et al. (2018), is used to calculate the Cauchy stress. The integration of the momentum equation in the total Lagrangian form (refer to the initial undeformed configuration) is given as:

$$\int \rho_s \frac{\partial^2\mathbf{D}}{\partial t^2} dV = \oint \left(J\mathbf{W}^{-T}\cdot\mathbf{n}\right)\cdot\boldsymbol{\sigma}\,dS + \int \rho_s\mathbf{g}\,dV \tag{6}$$

where ρ_s is the solid density, $\mathbf{D}$ is the displacement vector, $\mathbf{W}$ is the deformation gradient tensor given by $\mathbf{W} = \mathbf{I} + (\nabla\mathbf{D})^T$, $\mathbf{I}$ is the second-order identity tensor, J is Jacobian matrix of $\mathbf{W}$, i.e., det[$\mathbf{W}$], in which det[$\cdot$] is the determinant operator, and $\mathbf{n}$ is the outward facing normal vector. The Cauchy stress tensor $\boldsymbol{\sigma}$ is a nonlinear function of the displacement vector:

$$\boldsymbol{\sigma} = G\,\mathrm{dev}[J^{-2/3}\mathbf{W}\cdot\mathbf{W}^T] + \frac{\kappa}{2}\left(\frac{J^2-1}{J}\right)\mathbf{I} \tag{7}$$

where G and κ are the shear modulus and bulk modulus, respectively. They can be calculated by Young's modulus E and Poisson's ratio v:

$$G = \frac{E}{2(1+v)} \tag{8}$$

$$\kappa = \frac{E}{3(1-2v)} \tag{9}$$

2.3. Fully-coupled algorithm

A partitioned scheme is implemented for the interaction between the fluid and the solid domains. This means that the fluid and solid domains can be solved alternately, whilst the momentum and kinematic continuity at the fluid–solid interface is satisfied by a two-way coupling algorithm based on the Dirichlet–Neumann approach (Tuković et al., 2018). For all time steps, the pressure and velocity fields can first be obtained for the fluid domain. Then the fluid force is passed onto the solid interface where dynamic condition, i.e., force balance, is satisfied:

$$\mathbf{n}\cdot\boldsymbol{\sigma}_{\mathrm{fluid}} = \mathbf{n}\cdot\boldsymbol{\sigma}_{\mathrm{solid}} \tag{10}$$

where $\boldsymbol{\sigma}_{\mathrm{fluid}} = \boldsymbol{\tau} - p\mathbf{I}$ is the stress in the fluid domain. Thereby the solid domain can be solved with this Neumann condition (traction) at the interface boundary. Then, the velocity of the solid interface is passed back to the fluid interface using the Aitken under-relaxation approach, i.e., the relaxation factor varies in the FSI iterations to reduce the displacement residual faster. The fluid domain is therefore calculated with a Dirichlet condition of velocity at the interface boundary, satisfying the kinematic condition:

$$\mathbf{u}_{\mathrm{fluid}} = \mathbf{u}_{\mathrm{solid}} \tag{11}$$

Meanwhile, the mesh of the fluid domain is updated for the next iteration. A number of iterations are required for each time step to achieve a continuous displacement across the interface:

$$\mathbf{D}_{\mathrm{fluid}} = \mathbf{D}_{\mathrm{solid}} \tag{12}$$

A flowchart of the present fully-coupled FSI algorithm is illustrated in Fig. 1. In the present study, the tolerance of the displacement residual (i.e., the relative displacement between the fluid side and solid side interfaces) is specified as 1×10^{-6} m which is a negligible value compared with the magnitude of the displacement. Besides, the maximum number of FSI iterations per time step is set as 60, which allows the convergence to be achieved in each time step.

3. Model setup and boundary conditions

A two-dimensional numerical flume is established as shown in Fig. 2. The length and height of the flume are $10L$ and $2h$, respectively, in which L denotes the wavelength and h is the water depth. The numerical flume is built in a Cartesian coordinate system with x-axis pointing toward the wave propagation direction and z-axis toward the vertical direction. The origin of the coordinate system (O) is set at the center of the flume's bottom. A vertical wall is built in the center of the flume with a thickness of $h/15$ and a length (l) of $7h/6$, resulting in a freeboard height of $h/6$.

Three wave gauges represented by WG1–WG3 are placed upstream of the vertical wall. WG1 is at $x = -10h$ and the interval distances of WG1–WG2 and WG2–WG3 are $0.2L$ and $0.3L$, respectively. The reflected wave induced by the vertical wall is estimated by a wave reflection analysis method of Goda and Suzuki (1977) using the wave elevation records from wave gauges WG1–WG3. Moreover, a wave gauge WG4 is placed on the front side of the deformed wall. It moves along with the structural interface to observe the run-up which is

Table 1
Structural and wave properties in the present simulations.

Model	Mechanical properties					H (m)	T (s)
	ρ_s (kg/m^3)	E (GPa)	f_n (Hz)	γ	β		
1	1200	0.0120	2.640	0.08	0.10	0.04	0.6–1.6[a]
2	1200	0.0180	3.234	0.08	0.15		
3	1200	0.0240	3.734	0.08	0.20		
4	1200	0.0300	4.175	0.08	0.25		
5	1200	0.0360	4.573	0.08	0.30		
6	1200	0.0480	5.281	0.08	0.40		
7	1200	0.0720	6.468	0.08	0.60		
8	1200	0.1190	8.315	0.08	1.00		
9	1200	0.5950	18.592	0.08	5.00		
10	1800	35.760	117.687	0.12	30.0		

[a]Here the interval of the wave period is 0.2 s.

defined as the distance between the still water level and the maximum water level on the wall. To accurately evaluate the transmission coefficient (i.e., shoreward energy propagation), WG5–WG7 are placed downstream of the wall to perform the reflection analysis. Therefore, the evaluation of the transmission coefficient is not influenced by the wave reflection from the outlet boundary (5% on average). Besides, the horizontal wave loading per unit width of the wall F_x is obtained by integrating the pressure on the solid interface.

For the applicability of analysis, the mechanical properties of the wall are normalized into two non-dimensional parameters by the water depth. In particular, the mass coefficient of the vertical wall is defined as:

$$\gamma = \frac{\rho_s b}{\rho_w h} \tag{13}$$

where b is the thickness of the wall. The stiffness coefficient of the vertical wall is given by:

$$\beta = \frac{EI}{\rho_w g h^4} \tag{14}$$

where $I = b^3/12$ is the moment of inertia of the wall.

The present study is conducted on the model scale. The simulated structural and wave properties are listed in Table 1 with 60 cases in total. A series of wall models (i.e., Models 1–9) with different mechanical properties are considered for the present parametric investigation. The material stiffness gradually increases from Model 1 to Model 9, and Model 10 (almost rigid body) serves as a control group. The structural characterization can properly describe the structural responses under the wave loading (Dermentzoglou et al., 2021). Therefore, the corresponding natural frequency of the first mode for each model is obtained by the analytical solution for a cantilever beam, $f_n = \frac{k_n}{2\pi}\sqrt{\frac{EI}{\rho_s l^4}}$, where $k_n = 3.52$ (Young et al., 2012). The range of wave conditions modeled is given in Table 1 with a constant wave height $H = 0.04$ m, water depth $h = 0.3$ m, and a series of wave periods $T = 0.6$–1.6 s. The incident wave ranges from Stokes 2nd order to Stokes 3rd order before reaching the wall according to Le Méhauté (2013).

The boundary conditions are set as follows. In the fluid domain, the left and right sides of the flume are specified as wave inlet and wave outlet, respectively. Wave generation boundary with active wave absorption is applied at the wave inlet and waves are generated by the stream function theory (Fenton, 1988). Wave absorption boundary is applied at the wave outlet and the radiated waves stimulated by the oscillation of the wall can be effectively absorbed at the end of the numerical flume (for more details, see Higuera et al. (2013)). Note that we initially attempted to employ waves2Foam with the relaxation zone approach developed by Jacobsen et al. (2012) for the wave generation and absorption (as that has been used in Li et al. (2018, 2020) for rigid structures). However, our generated wave height could not reach the targeted value during propagation with mesh deformation. Instead, we incorporated the wave generation and absorption technique in IHFOAM

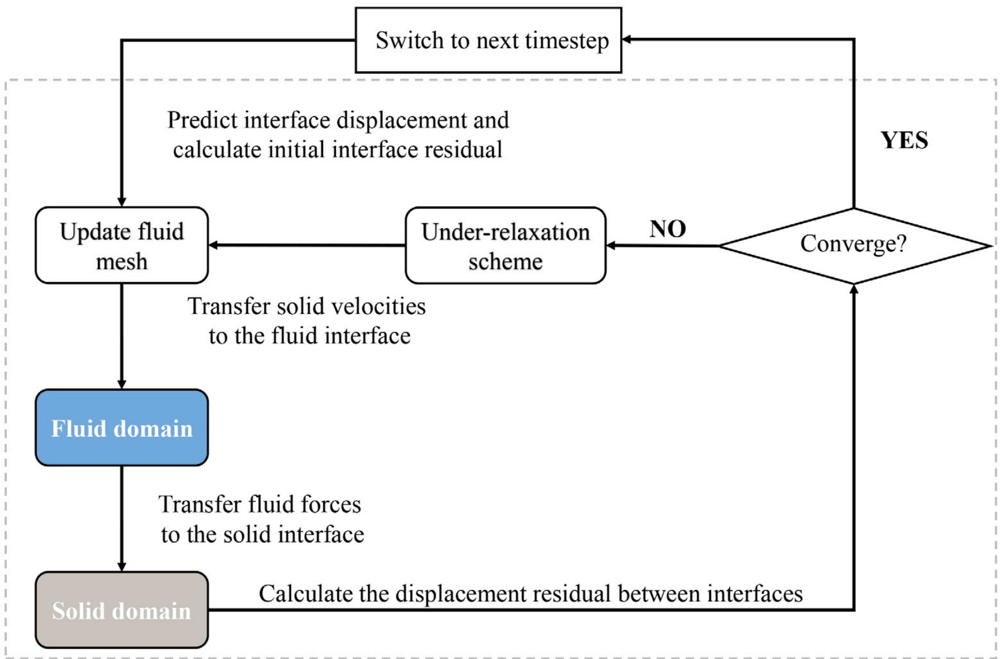

Fig. 1. Flowchart of FSI coupling algorithm.

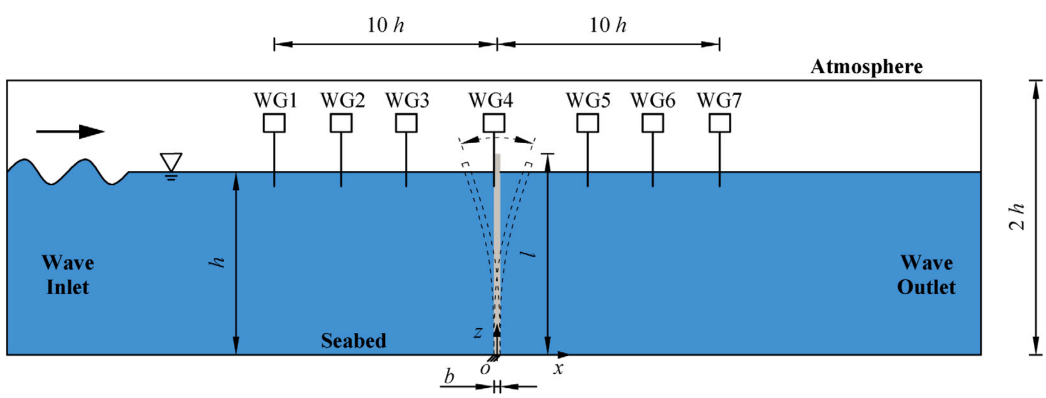

Fig. 2. Schematic diagram of the numerical flume (not to scale).

(using active wave absorption to cancel out the reached waves on the boundaries) and were able to achieve accurate and stable wave propagation when combined with moving mesh. The bottom and the top are set as no-slip wall and atmospheric boundary conditions, respectively. The interfaces with solid are set as the Dirichlet boundary condition for the velocity (see Eq. (11)). In the solid domain, the interfaces with fluid are specified as the Neumann boundary condition for the traction (see Eq. (10)). The bottom of the wall is set as a fixed-support boundary condition and keeps clamped under the wave loading.

The present fully-coupled model is based on a cell-centered finite volume method. Spatial and temporal discretizations are introduced in the computational simulation with a non-overlapping structured hexahedral mesh and finite time steps. In particular, the spatial domain consists of the fluid sub-domain and the solid sub-domain, which can simultaneously represent the evolution of the fluid and the structure. The governing equations (Eqs. (1) and (2)) can be numerically solved using specified initial and boundary conditions. The Pressure Implicit with Splitting of Operators (PISO) algorithm (Issa, 1986) is applied to decouple the $p - \mathbf{u}$ equations and iteratively solve them. Time integration is determined by the Courant–Friedrichs–Lewy (CFL) criteria. The simulations are performed with a fixed time step $\Delta t = 0.001$ s, which ensures the Courant number $Co \leq 0.1$ for wave propagation and $Co \leq 0.2$ near the structure as the wave orbital velocity increases due to the reflection. The passage of 30 waves per simulation case takes approximately 2 days using 12 processors on the supercomputer of the National Supercomputing Centre (NSCC).

4. Model verification

4.1. Verification against solitary wave interaction with an elastic wall

Detailed validations for the present model have been conducted in Huang and Li (2022) for an elastic submerged horizontal plate in nonlinear waves. For the present study involving a vertical elastic wall in periodic waves, there was no experimental study in the open literature. The present model was thereby adequately verified against the numerical results of He and Kashiwagi (2012), who investigated the hydroelastic behavior of a vertical cantilever wall in a solitary wave. Their work was well validated against the analytical result of Peter and Meylan (2010) and another numerical simulation based on a mode-expansion method (He and Kashiwagi, 2009). Recently, their results were also verified by Akrish et al. (2018). Therefore, their model results are seeming to be reliable for our verification purposes.

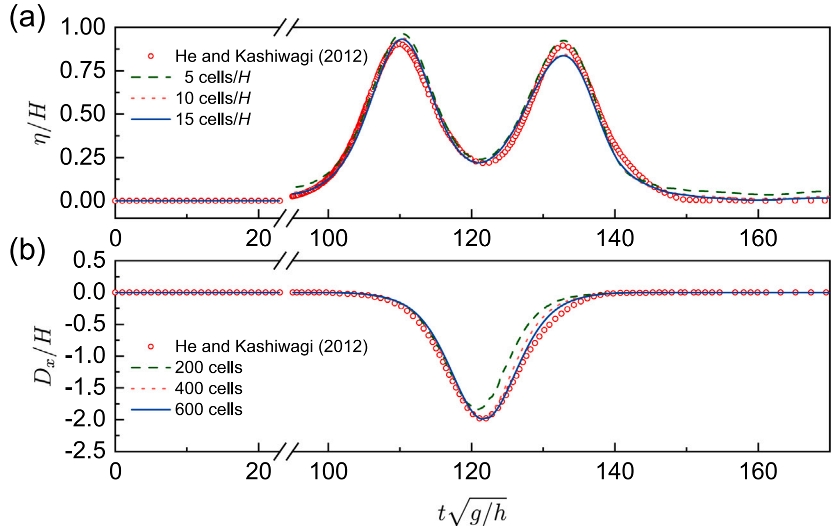

Fig. 3. Comparison of the normalized (a) wave elevation at $x = -10h$ and (b) horizontal displacement of the wall at $z = h/2$ between the present simulation and He and Kashiwagi (2012).

In this subsection, the case of the top-free wall was simulated with different cell sizes for the fluid domain and the solid domain. A solitary wave with a wave height of $0.04h$ was generated at $x = -50h$. The mass coefficient γ and the stiffness coefficient β of the wall are 0.01 and 0.04, respectively. The height of the wall is $1.1h$ and the normalized time duration $t\sqrt{g/h}$ is 180 in this verification simulation, in which the water depth is again set as $h = 0.3$ m. For comparison, the wave elevation η/H at $x = -10h$ and the horizontal displacement D_x/H of the wall at $z = h/2$ were recorded.

Three sets of mesh with 5, 10, and 15 cells per wave height were employed. The aspect ratio of the cells was set as 1/3 (i.e., cell height/cell width), which conformed to the range proposed in Jacobsen et al. (2014). The simulated results show good agreement with (He and Kashiwagi, 2012) as seen in Fig. 3a. A small drop in our simulated reflected wave occurs at $t\sqrt{g/h} = 132.8$. It is because the deformation of the wall transfers the wave energy downstream, which is not considered in He and Kashiwagi (2012). It is found that the result of 10 cells/H is almost identical to that of 15 cells/H, while the result of 5 cells/H slightly overestimates the wave elevation. Therefore, the mesh set with 10 cells per wave height is adopted for what follows in this subsection. The horizontal displacement of the wall at $z = h/2$ is verified using three different sets of solid mesh with 200, 400, and 600 cells (i.e., 2×100, 4×100, and 6×100 cells in the horizontal and vertical directions). In Fig. 3b, the result of 400 cells is fairly close to that of 600 cells, which achieves convergence. However, the displacement of 200 cells is notably lower, especially near the peak value. The mesh set of 400 cells is seen to provide an accurate and efficient solution, therefore is used for the solid domain in the following simulations.

4.2. Validation against periodic waves interaction with a rigid wall

Section 4.1 provided the verification on a solitary wave. As the present study focuses on the periodic waves, the numerical model was validated against the experiment of Didier et al. (2014) for regular waves impacting on a vertical rigid wall. The numerical simulations were conducted with the identical setup as in Didier et al. (2014). A non-breaking wave case with $H = 0.1$ m, $T = 1.3$ s, and $h = 0.325$ m was selected for the present validation. Three densities of mesh (i.e., 10, 15, and 20 cells per wave height with an aspect ratio of 1/3) were tested for the grid convergence study. Fig. 4a shows the comparison of the wave elevation at 2.643 m from the wave-maker initial position. All sets of the mesh give satisfactory predictions compared to the laboratory measurement. The mesh of 15 cells/H shows nearly identical results as the mesh of 20 cells/H and slightly more accurate results compared to the mesh of 10 cells/H. Fig. 4(b–c) show the pressure at 0.055 m and 0.165 m above the bottom of the wall, respectively. A good agreement is globally observed between numerical and experimental results. Note that the maximum pressure in the simulation is larger than the experiment, which is due to an insufficient data sampling rate at the experimental tests, as reported in Didier et al. (2014). Based on the above results, the mesh set with 15 cells per wave height is used for the following simulations. The utilized final mesh with a zoom-in view is shown in Fig. 5, where the fluid interface is conformal to the solid interface to minimize the interpolation error at boundaries.

5. Results and discussion

Detailed investigations of waves interacting with an elastic wall in terms of hydrodynamic characteristics, structural dynamic responses, structural optimization, and material damping effect are presented in the following subsections.

5.1. Hydrodynamic characteristics

5.1.1. Reflection and transmission coefficients

To investigate the energy propagation of waves interacting with the elastic wall, the reflection coefficient (C_r, i.e., the ratio of the reflected wave height to the incident wave height) and the transmission coefficient (C_t, i.e., the ratio of the radiated wave height caused by the oscillation of the wall to the incident wave height) against the stiffness coefficient β are analyzed and shown in Fig. 6. The rigid wall (i.e., $\beta = 30$) presents a perfect reflection with no transmission despite the changes in wave steepness (H/L). For the elastic walls, as β increases from 0.10 to 5, C_r gradually increases whilst C_t decreases. This trend is more obvious when the value of β is relatively small. Besides, it is seen that C_r is with an increasing tendency against the increase of the wavelength L (corresponding to the decrease of H/L), especially for the smaller β, indicating that longer waves are easier to be reflected by elastic walls. It is worthwhile to mention that the value of $C_r^2 + C_t^2$ is close to 1 for all scenarios, which implies that the total reflected and transmitted wave energy is approximately equal to the incident wave energy with negligible energy dissipation. Thereby, the increase of C_r naturally leads to the decrease of C_t for each model.

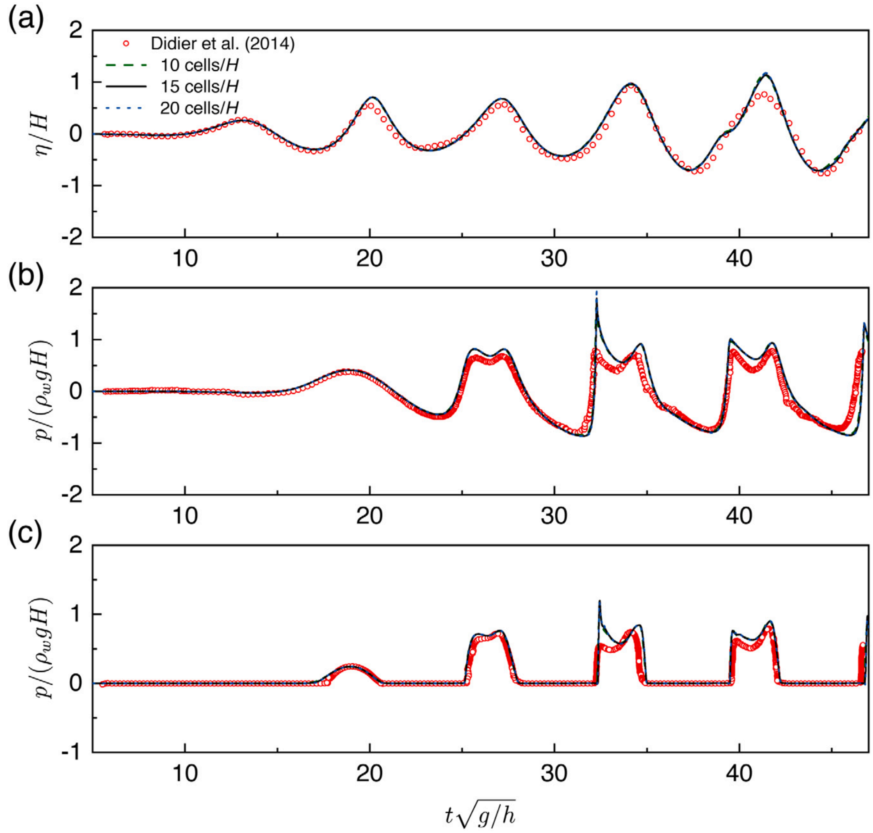

Fig. 4. Comparison of the normalized (a) wave elevation at 2.643 m from the wave-maker initial position, (b) pressure at 0.055 m above the bottom of the wall, and (c) pressure at 0.165 m above the bottom of the wall.

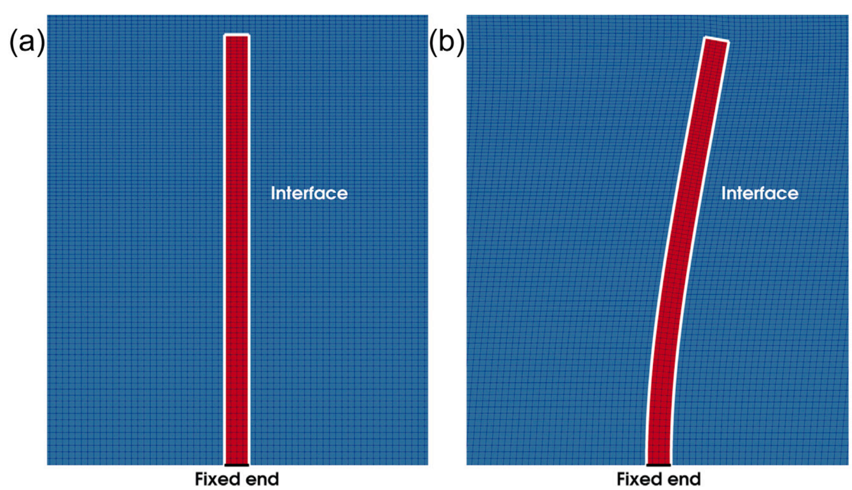

Fig. 5. The zoom-in view of the (a) undeformed and (b) deformed mesh with blue denoting the fluid domain and red denoting the solid domain. The white line represents the interface between the fluid and solid, and the black line at the bottom represents the fixed end of the wall.

5.1.2. Wave run-up and loading

Besides C_r and C_t, other important considerations are the wave run-up and loading on the wall with various stiffness coefficients. The wave run-up R (nondimensionalized by H) and the horizontal peak force per unit width $F_{x,max}$ (nondimensionalized by $\rho_w ghH$) exerted on the wall are shown in Fig. 7. For both the rigid and elastic walls, the normalized wave run-up R/H increases with the wavelength L, as illustrated in Fig. 7a. This is because the longer waves have larger wave excursion, $A_w = u_{x,max}T/2\pi$, where $u_{x,max}$ is the maximum horizontal velocity of the fluid particle. A_w increases from 0.020 m to 0.036 m as the wavelength L increases from 0.56 m to 2.53 m (corresponding to H/L decreases from 0.071 to 0.016). Besides, R/H gradually increases with β and the gradient is negligible when $\beta > 1$, which is similar to the tendency of C_r. Fig. 7b shows that the normalized $F_{x,max}$ also increases with β and L, while the change of the wavelength makes a bigger difference of $F_{x,max}$ especially for the rigid wall. The increases of both the wave run-up and loading against β are due to the enhanced wave reflection causing a higher wave elevation on the wall when superimposed with the incident wave. Therefore, the dynamic pressure on the wall can be increased with the wave reflection, which causes a higher pressure difference between the front and back of the

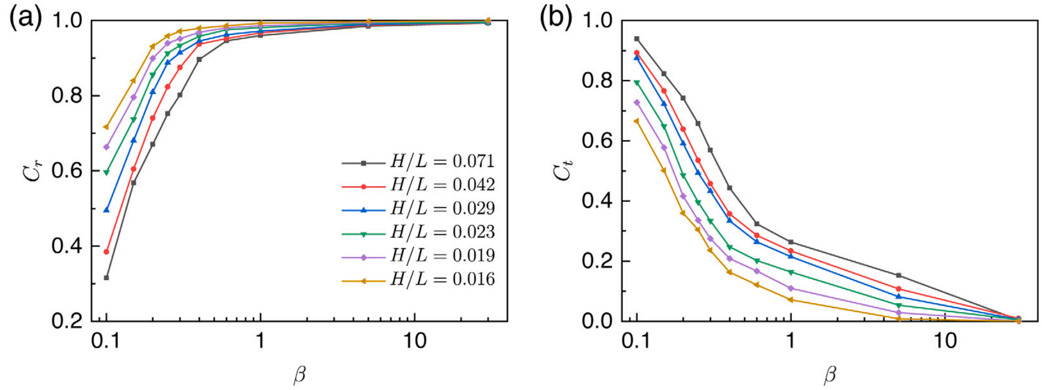

Fig. 6. Comparisons of (a) reflection coefficient and (b) transmission coefficient induced by walls with different stiffness coefficients β.

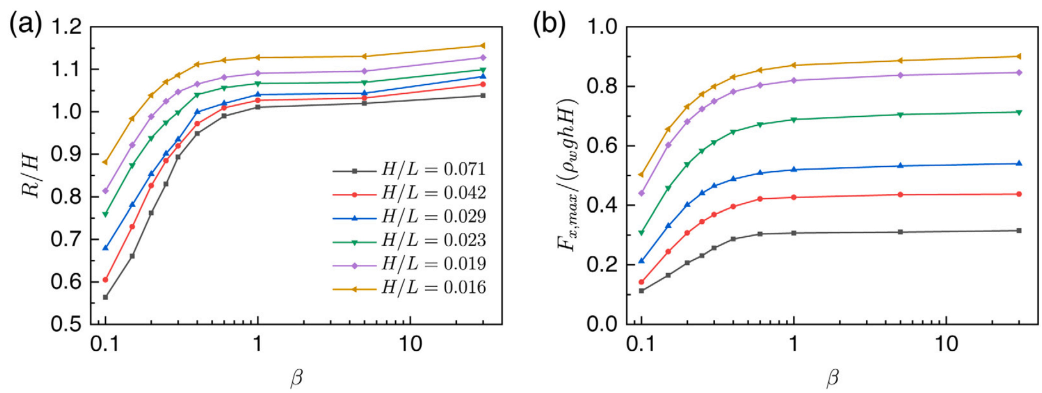

Fig. 7. Comparisons of (a) wave run-up and (b) horizontal peak wave force between walls with different stiffness coefficients β.

wall. Compared with the rigid wall, the introduction of flexibility can significantly reduce the wave run-up and loading on the wall.

The predictions of the wave run-up and horizontal peak force are of great importance for the design and optimization of flexible structures in coastal engineering. Previous studies showed a linear dependence of the normalized run-up on the wave steepness (Hunt, 1959):

$$\frac{R_{pred}}{H} = a\left(\frac{H}{L}\right)^c \tag{15}$$

For the wave run-up estimation on vertical elastic structures, the stiffness coefficient β describing the flexural rigidity should also be considered in addition to the wave steepness. Therefore, we propose a modified equation for the prediction of the wave run-up on a vertical elastic wall as follows:

$$\frac{R_{pred}}{H} = a\left(\frac{1}{1+\frac{1}{k\beta}}\right)\left(\frac{H}{L}\right)^c \tag{16}$$

where R_{pred} is the predicted wave run-up, a, k, and c are the empirical coefficients. This form of the formula allows it to revert to that for rigid structures (Eq. (15)) when β is very large. A wide range of wall stiffness and wave conditions are calibrated in Fig. 8a for the best fitting, resulting in $a = 0.697$, $k = 20.629$, and $c = -0.132$. The empirical formula (Eq. (16)) successfully captures the numerical results with a coefficient of determination of 0.894. Most of the cases lie within ±6% deviations. Likewise, the predicted horizontal peak force exerted on the wall per unit width $F_{x,max,pred}$ can be obtained by:

$$\frac{F_{x,max,pred}}{\rho_w g h H} = a\left(\frac{1}{1+\frac{1}{k\beta}}\right)\left(\frac{H}{L}\right)^c \tag{17}$$

Forces calculated by Eq. (17) with $a = 0.033$, $k = 12.799$, and $c = -0.815$ are compared with numerical results in Fig. 8b. It provides good estimations with a coefficient of determination of 0.962. These modified prediction formulae can provide the evaluations for the wave run-up and loading of vertical elastic structures.

5.2. Dynamic response of the wall

5.2.1. Displacement of the wall

To further investigate the structural response of the elastic wall in periodic waves, the horizontal displacement of the wall is analyzed. Fig. 9 shows the comparisons between the wave elevation η at the front face of the moving wall, horizontal wave force F_x, and the horizontal displacement at the free top D_x during two wave cycles with $H/L = 0.016$. For Model 2 (see Fig. 9a), an approximately $0.06T$ phase lag is observed between D_x and η. Thereby D_x slightly lags behind the wave force. Note that the amplitudes of the crest and trough are slightly asymmetric for η, F_x, and D_x because of the superposition of higher-order nonlinear wave components. In Fig. 9b, the signals in the time domain are decomposed into the components of the fundamental frequency and higher harmonics using a fast Fourier transform (FFT), where the frequencies are normalized by the incident wave frequency (f_w). It is observed that D_x has the same frequency as that of the incident wave loading. Besides, the amplitude of D_x is predominant at the fundamental frequency, with a minor role in the 2nd harmonic, and negligible in the 3rd and 4th harmonics, which is determined by the wave excitation. Fig. 9(c–d) present the results of Model 5 in the same wave condition. With a larger β, the abovementioned phase lag between D_x and η tends to decrease to about $0.02T$, which implies the wall displacement becomes more synchronous with the exerted wave elevation as well as the wave loading. As expected, the vibration frequency is again the same as the wave force, independent of the wall properties.

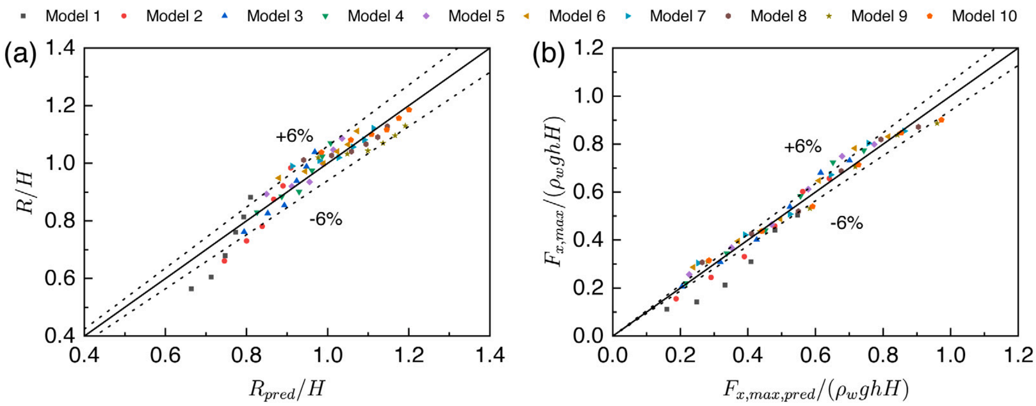

Fig. 8. Comparisons of the predicted (a) wave run-up obtained by Eq. (16) and (b) horizontal peak wave force obtained by Eq. (17) with numerical results.

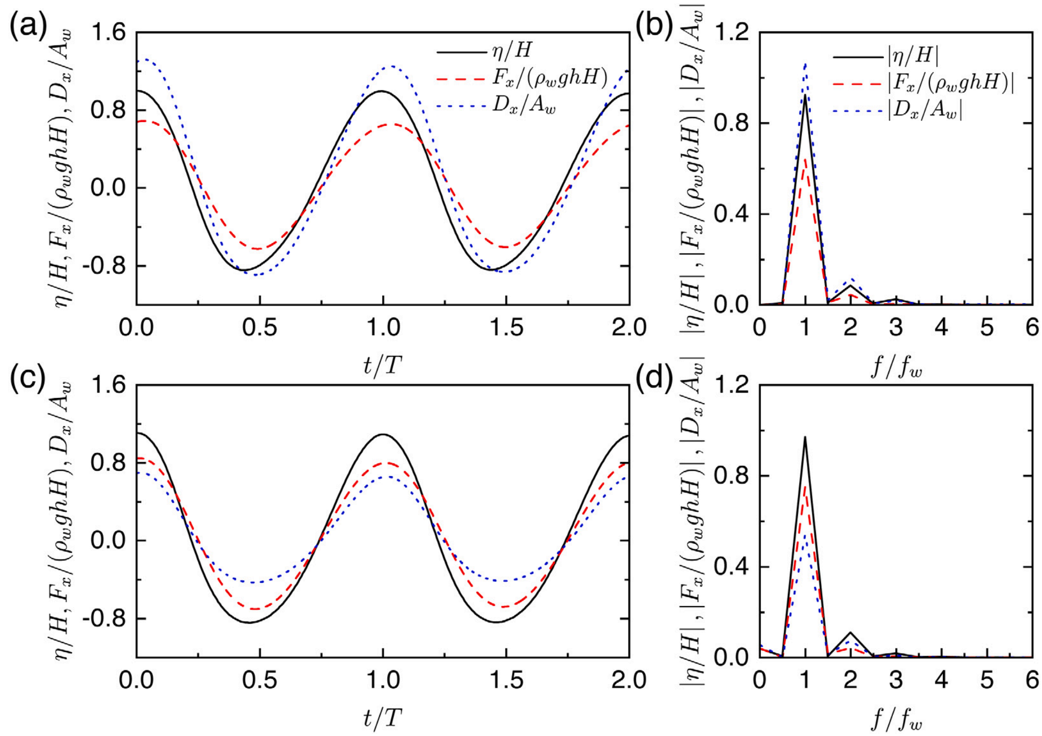

Fig. 9. Time series and the corresponding amplitude spectrum of the wave elevation, horizontal wave force, and horizontal displacement of the wall for (a–b) Model 2 and (c–d) Model 5 in waves with $H/L = 0.016$.

Fig. 10a presents the horizontal maximum displacement $D_{x,max}$ (nondimensionalized by the wave excursion A_w) against the ratio of the incident wave frequency to the natural frequency of the wall, f_w/f_n. It is obvious that $D_{x,max}/A_w$ rapidly increases with f_w/f_n under the same wave condition. This increase is more significant for waves with a smaller H/L and the structure with a larger f_w/f_n. However, for the same structure (connected by dotted lines), a peak of $D_{x,max}/A_w$ seems to appear at waves with $H/L = 0.019$. Given the same dimensionless parameters as that in Eqs. (16) and (17), the predicted horizontal maximum displacement $D_{x,max,pred}$ can be directly obtained by the following formula:

$$\frac{D_{x,max,pred}}{A_w} = a\left(\frac{1}{1+k\beta}\right)\left(\frac{H}{L}\right)^c \tag{18}$$

As shown in Fig. 10b, $D_{x,max,pred}$ predicted by Eq. (18) with $a = 1.872$, $k = 17.210$, and $c = -0.221$ almost coincide with the numerical results with a coefficient of determination of 0.984. Most of the data lie within the ±6% derivations. Therefore, the proposed empirical formula can provide satisfactory estimations for the displacement of the elastic wall in a certain range of wave conditions and material stiffness.

5.2.2. Von Mises stress in the wall

Figs. 11–13 present snapshots of the free surface (denoted by blue contours) together with the bending deflection as well as the von Mises stress σ_v (nondimensionalized by $\rho_w g H$) in the wall under wave loading. For Model 1 in periodic waves with $H/L = 0.029$ and $f_w/f_n = 0.379$, a phase lag is seen between the structural displacement and the wave elevation, i.e., the horizontal maximum displacement $D_{x,max}$ (i.e., shoreward displacement amplitude) occurs at $t = 0.14T$ instead of at the wave crest (see Fig. 11a). At this moment, the pressure difference between the upstream and downstream sides lead to the peak σ_v during the whole wave cycle. The relatively high stress is concentrated near the toe, with a maximum stress $\sigma_{v,max}$ at the rear side of the wall. In the vertical direction, σ_v gradually decreases to zero from the bottom to the free top. As waves propagate, the minimum horizontal displacement $D_{x,min}$ (i.e., seaward displacement amplitude) of the wall occurs at

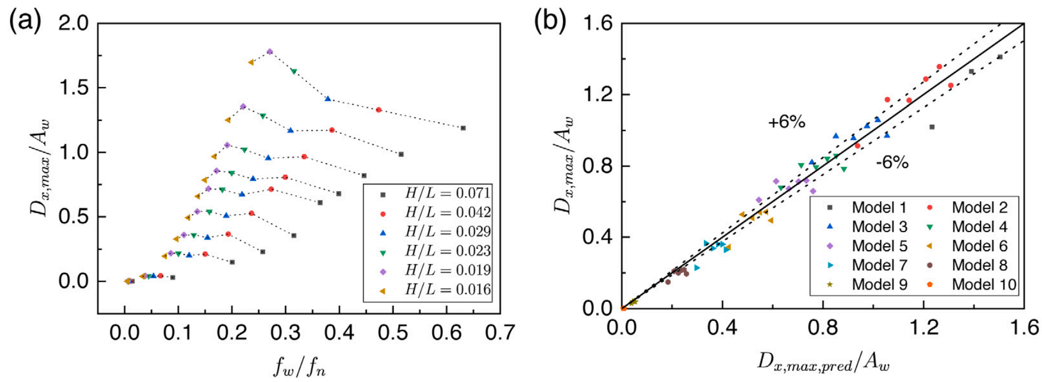

Fig. 10. Comparison of the horizontal maximum displacement between (a) cases with different frequency ratios and (b) the predicted and numerical results.

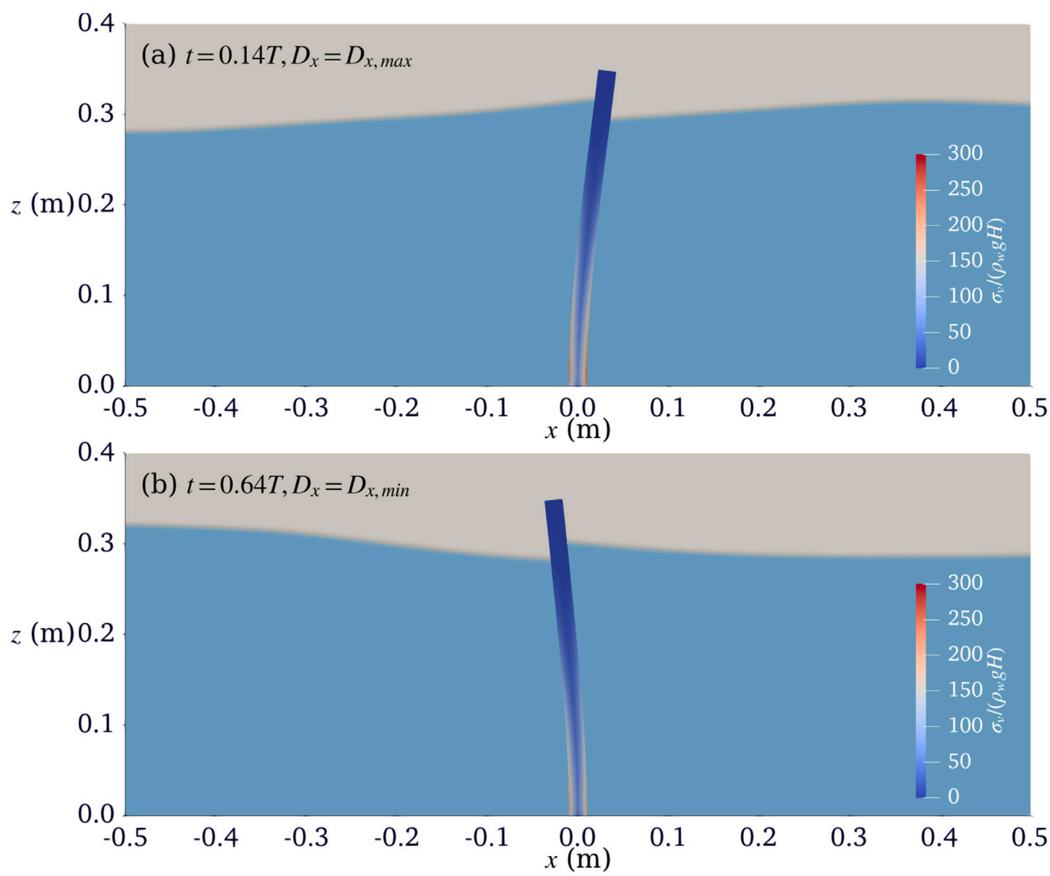

Fig. 11. Snapshots of periodic waves with $H/L = 0.029$ on Model 1 at (a) $D_x = D_{x,max}$ and (b) $D_x = D_{x,min}$.

$t = 0.64T$ (see Fig. 11b). σ_v in Fig. 11b is slightly smaller than that in Fig. 11a, which is more obvious at the rear toe of the wall. This is again due to wave nonlinearity, where the fluid moves faster at the wave crest than the wave trough (Dean and Dalrymple, 1991).

Fig. 12 shows the results of Model 2 with a larger stiffness coefficient. Comparing Fig. 12 and Fig. 11, as f_w/f_n decreases from 0.379 to 0.309, σ_v in the wall increases under both wave forth and back loadings, especially near the toe of the wall. This is because the restoring force caused by the stiffness becomes more dominant compared with the hydrodynamic force. Note that the abovementioned phase lag between the wall displacement and the wave elevation decreases to about $0.10T$ with the decrease of f_w/f_n. Fig. 13 shows the results of Model 2 in waves with a smaller H/L. Comparing Fig. 13 and Fig. 12, as H/L decreases from 0.029 to 0.016, f_w/f_n decreases from 0.309 to 0.193. It can be found that the von Mises stress further significantly increases. However, the phase lag between η and D_x decreases to $0.06T$ with the decrease of f_w/f_n.

5.3. Optimal design conditions of the flexible wall

As discussed above, the change of the frequency ratio f_w/f_n and the wave steepness H/L can significantly affect the wave evolution and the structural integrity. A stiffer structure can have larger wave-induced stresses in the wall, which has negative impact on the structural integrity. However, the decrease of the structural stiffness (i.e., more flexible) can intensify the shoreward energy transmission, which can exacerbate coastal vulnerability (Jin et al., 2015). Therefore, a design balance should be considered when incorporating the flexibility of the wall. In the present study, a preliminary optimization of the flexibility is conducted to balance the defense performance and structural integrity.

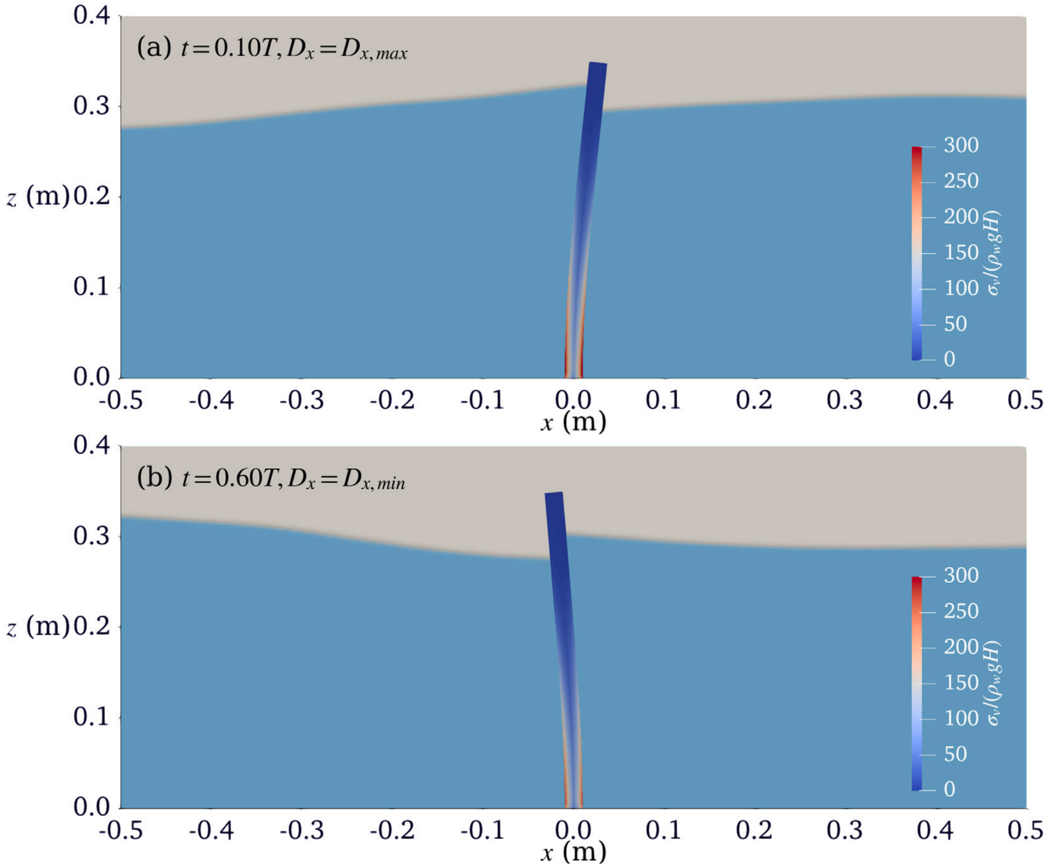

Fig. 12. Snapshots of periodic waves with $H/L = 0.029$ on Model 2 at (a) $D_x = D_{x,max}$ and (b) $D_x = D_{x,min}$.

In the optimization, minimizing transmission coefficient C_t is chosen as one objective for improving the defense performance while minimizing maximum von Mises stress $\sigma_{v,max}$ is another objective for ensuring the integrity of the wall. We know from the parametric study above that these two objectives conflict with each other. Thereby optimal decisions need to be taken in the presence of trade-offs between them. Meanwhile, there are also many other considerations e.g. the cost, which are not included in the present optimization scope. Fig. 14a shows the contour of C_t against f_w/f_n and H/L. It is seen that the smallest C_t distributes in the space with small f_w/f_n and H/L. The transmission coefficient seems to be almost uniform for a specific f_w/f_n. To ensure low wave transmission ($C_t < 0.5$, i.e., 75% energy cutoff), $f_w/f_n < 0.25$ can be an optimal choice. Therefore, we can focus on the single objective of minimizing $\sigma_{v,max}$. Fig. 14b shows a nearly opposite trend of $\sigma_{v,max}$ against f_w/f_n and H/L. It is noted that for relatively longer waves ($0.016 < H/L < 0.029$) and smaller frequency ratio ($f_w/f_n < 0.25$), $\sigma_{v,max}$ in the wall is extreme large (Fig. 14b). The decrease in wavelength (corresponding to the increase of H/L) can significantly reduce the stress in the structure. $H/L > 0.029$ results in $\sigma_{v,max}/\rho_w gH$ almost smaller than 300, thereby can be considered as an optimal choice for this range of wave steepness. Therefore, The area of $H/L > 0.029$ and $f_w/f_n < 0.25$ could be an optimal choice for design balance. Note that optimal solutions are dependent on the relative importance of the objectives, which can lead to different solutions in different applications.

5.4. The effect of the material damping

As an effective-damping material, rubbers can restrain the vibratory motion by dissipating the energy. As the aforementioned study did not consider material damping, in this section, we aim to study how much material damping can affect the interaction between periodic waves and an elastic wall. To consider the material damping, an additional term (i.e., $c_s \int \rho_s \frac{\partial \mathbf{D}}{\partial t} dV$) is added at the left hand side of Eq. (6), in which c_s is the constant viscous damping coefficient of the material. An approximate damping coefficient $c_s = 0.15\ s^{-1}$ of rubber is introduced herein with reference to the quantification of Lin et al. (2005).

Here we present the results for Model 1 in waves with $H/L = 0.023$ as an example. The dimensionless wave elevation of WG4, horizontal displacement of the free top, and horizontal force per unit width exerted on the wall with ($c_s = 0.15\ s^{-1}$) and without ($c_s = 0\ s^{-1}$) material damping are compared in Fig. 15. It can be found that the two curves coincide with each other in all subplots, which indicates that the material damping does not affect the hydrodynamic characteristics and structural responses of the elastic wall in periodic waves. This is because the loading of ocean waves is continuous and with low frequency. Therefore the damping term is proportional to a very low deformation rate (i.e., small $\frac{\partial \mathbf{D}}{\partial t}$), resulting in a negligible damping effect compared to the wave loading. As a result, the material damping can be ignored in simulations leading to related problems. This corroborates the discussion given in Huang and Li (2022), in which the authors inferred that the material damping has negligible influence on the hydroelastic wave–structure interaction. However, the damping effect for the impact of other environmental loads, e.g., seismic loads may still need to be considered.

6. Conclusions

The present study performed a systematic investigation of the hydroelastic behavior of a wall in periodic waves using a fully-coupled wave–structure interaction model. The main conclusions in this study are drawn as follows:

(1) In contrast to a rigid wall with perfect reflection, a remarkable reduction is observed in wave reflection with an increased wave

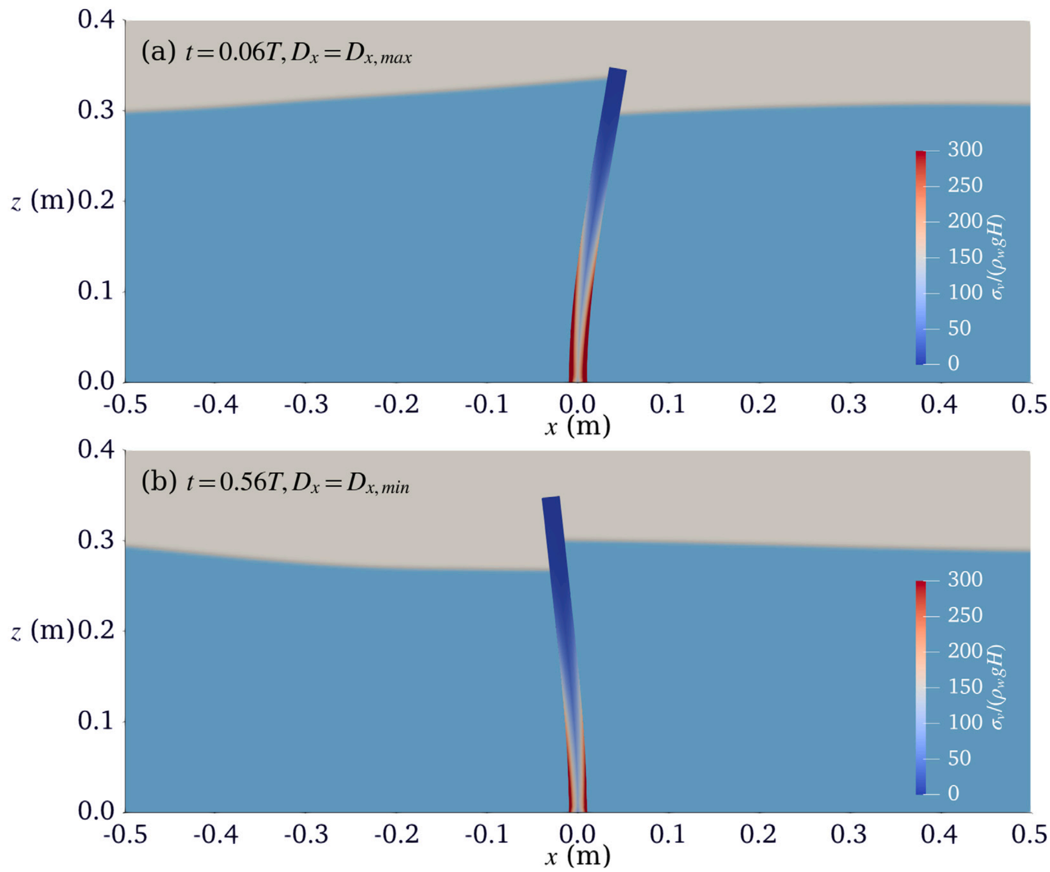

Fig. 13. Snapshots of periodic waves with $H/L = 0.016$ on Model 2 at (a) $D_x = D_{x,max}$ and (b) $D_x = D_{x,min}$.

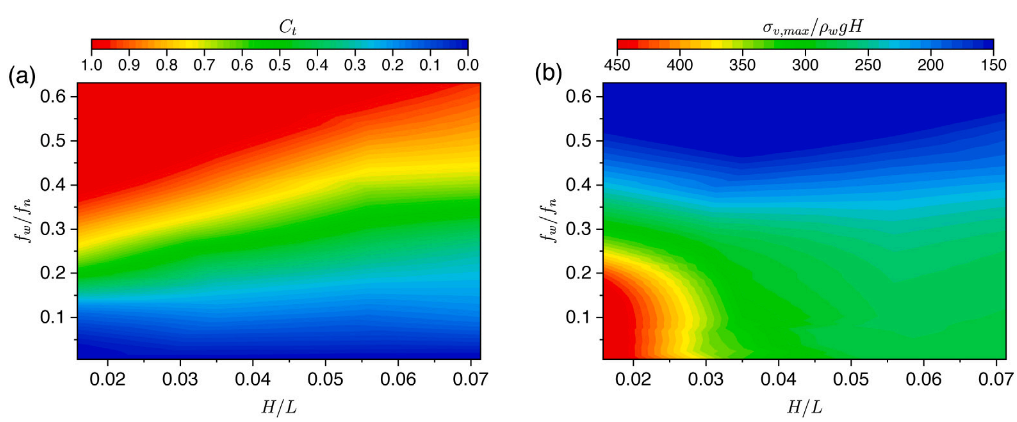

Fig. 14. Contours of (a) transmission coefficient and (b) maximum von Mises stress against the frequency ratio and the wave steepness.

transmission for the applied elastic wall. This is more obvious for more flexible walls.

(2) Higher flexibility of the wall is observed to significantly reduce the wave run-up and loading. Modified empirical formulae are proposed for the predictions of run-up and maximum wave loading by introducing the effect of structural flexibility, which provides quick estimations for the results obtained through time-consuming simulations. This can be particularly useful in early-stage design processes.

(3) A slight phase lag is observed between the horizontal displacement of the elastic wall and the exerted wave loading. It increases with the ratio of the incident wave frequency to the wall's natural frequency. The structural response has the same frequency as that of the wave force. An empirical formula is also proposed for the prediction of the maximum displacement.

(4) The normalized von Mises stress in the wall increases with the decrease of the ratio of the incident wave frequency to the wall's natural frequency. The relatively high stresses are concentrated near the toe of the wall, with maximum stress at the rear toe of the wall. Similar to the wall displacement, the stress is larger in the shoreward direction than those in the seaward direction.

(5) The optimization of the flexible wall is studied taking into account both the defense performance and the structural integrity. Besides, material damping is proved to have a negligible effect on the interaction between periodic waves and an elastic wall.

The present work aims to support the design and optimization of an elastic wall interacting with periodic waves. More experimental data are required to fully validate the design and optimizations. Meanwhile, the present model (released in the next section) should a useful tool for

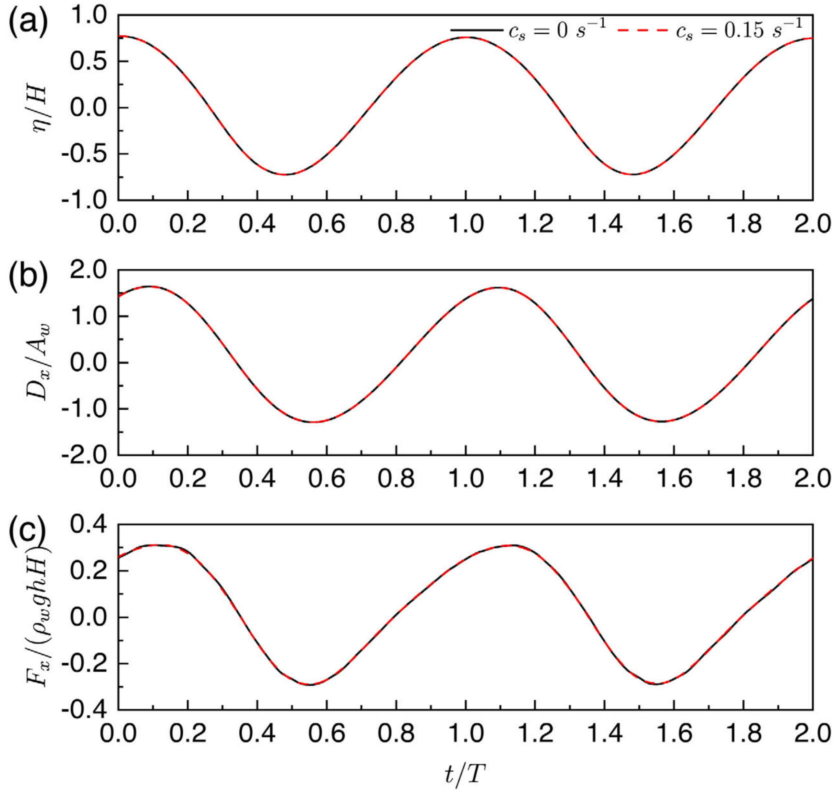

Fig. 15. Comparison of the normalized (a) wave elevation, (b) horizontal displacement at the free top, and (c) horizontal force exerted on walls with and without material damping.

predicting the interaction between ocean waves and flexible structures in the coastal and offshore regions.

Availability of source codes

The source code implemented and utilized in the present work is publicly available at: https://github.com/huzhengyu/wave2solids. The fully-coupled wave–structure interaction code is developed in OpenFOAM version foam-extend-4.0. The present simulation for the elastic wall in periodic waves is provided as a tutorial.

CRediT authorship contribution statement

Zhengyu Hu: Investigation, Data curation, Writing – original draft, Code development. **Luofeng Huang:** Code development assistance, Writing – review & editing, Methodology. **Yuzhu Li:** Conceptualization, Methodology, Writing – review & editing, Supervision, Supercomputer resources acquisition, Funding acquisition.

Declaration of competing interest

The authors declare that they have no known competing financial interests or personal relationships that could have appeared to influence the work reported in this paper.

Data availability

The source code implemented and utilized in the present work is publicly available at: https://github.com/huzhengyu/wave2solids. The fully-coupled wave–structure interaction code is developed in OpenFOAM version foam-extend-4.0. The present simulation for the elastic wall in periodic waves is provided as a tutorial.

Acknowledgment

This study was supported in part with computational resources provided by the National Supercomputing Centre, Singapore (https://www.nscc.sg), under Project ID: 11002459.

References

Akrish, G., Rabinovitch, O., Agnon, Y., 2018. Hydroelasticity and nonlinearity in the interaction between water waves and an elastic wall. J. Fluid Mech. 845, 293–320. http://dx.doi.org/10.1017/jfm.2018.207.

Attili, T., Heller, V., Triantafyllou, S., 2021. A numerical investigation of tsunamis impacting dams. Coast. Eng. 169, 103942. http://dx.doi.org/10.1016/j.coastaleng.2021.103942.

Cardiff, P., Karač, A., De Jaeger, P., Jasak, H., Nagy, J., Ivanković, A., Tuković, Ž., 2018. An open-source finite volume toolbox for solid mechanics and fluid-solid interaction simulations. arXiv preprint arXiv:1808.10736.

Dean, R.G., Dalrymple, R.A., 1991. Water Wave Mechanics for Engineers and Scientists, Vol. 2. world scientific publishing company.

Dermentzoglou, D., Castellino, M., De Girolamo, P., Partovi, M., Schreppers, G.-J., Antonini, A., 2021. Crownwall failure analysis through finite element method. J. Mar. Sci. Eng. 9 (1), 35. http://dx.doi.org/10.3390/jmse9010035.

Didier, E., Neves, D., Martins, R., Neves, M., 2014. Wave interaction with a vertical wall: SPH numerical and experimental modeling. Ocean Eng. 88, 330–341. http://dx.doi.org/10.1016/j.oceaneng.2014.06.029.

Fenton, J.D., 1988. The numerical solution of steady water wave problems. Comput. Geosci. 14 (3), 357–368. http://dx.doi.org/10.1016/0098-3004(88)90066-0.

Field, C.B., Barros, V.R., 2014. Climate Change 2014–Impacts, Adaptation and Vulnerability: Regional Aspects. Cambridge University Press.

Goda, Y., Suzuki, Y., 1977. Estimation of incident and reflected waves in random wave experiments. In: Proceedings of the 15th International Conference on Coastal Engineering ASCE1976. pp. 828–845. http://dx.doi.org/10.1061/9780872620834.048.

He, G., Kashiwagi, M., 2009. Nonlinear solution for vibration of vertical plate and transient waves generated by wave impact. Int. J. Offs. Polar Eng. 19 (03).

He, G., Kashiwagi, M., 2012. Numerical analysis of the hydroelastic behavior of a vertical plate due to solitary waves. J. Mar. Sci. Technol. 17 (2), 154–167. http://dx.doi.org/10.1007/s00773-011-0155-9.

Higuera, P., Lara, J.L., Losada, I.J., 2013. Realistic wave generation and active wave absorption for Navier–Stokes models: Application to OpenFOAM®. Coast. Eng. 71, 102–118. http://dx.doi.org/10.1016/j.coastaleng.2012.07.002.

Hirt, C.W., Nichols, B.D., 1981. Volume of fluid (VOF) method for the dynamics of free boundaries. J. Comput. Phys. 39 (1), 201–225. http://dx.doi.org/10.1016/0021-9991(81)90145-5.

Hsiao, S.-C., Lin, T.-C., 2010. Tsunami-like solitary waves impinging and overtopping an impermeable seawall: Experiment and RANS modeling. Coast. Eng. 57 (1), 1–18. http://dx.doi.org/10.1016/j.coastaleng.2009.08.004.

Huang, L., Li, Y., 2022. Design of the submerged horizontal plate breakwater using a fully coupled hydroelastic approach. Comput.-Aided Civ. Infrastruct. Eng. 37 (7), 915–932. http://dx.doi.org/10.1111/mice.12784.

Huang, L., Li, Y., Benites-Munoz, D., Windt, C.W., Feichtner, A., Tavakoli, S., Davidson, J., Paredes, R., Quintuna, T., Ransley, E., Colombo, M., Li, M., Cardiff, P., Tabor, G., 2022. A review on the modelling of wave-structure interactions based on OpenFOAM. OpenFOAM® J. 2, 116–142. http://dx.doi.org/10.51560/ofj.v2.65.

Huang, L., Ren, K., Li, M., Tuković, Ž., Cardiff, P., Thomas, G., 2019. Fluid-structure interaction of a large ice sheet in waves. Ocean Eng. 182, 102–111. http://dx.doi.org/10.1016/j.oceaneng.2019.04.015.

Hunt, I.A., 1959. Design of seawalls and breakwaters. J. Waterw. Harb. Div. 85 (3), 123–152. http://dx.doi.org/10.1061/JWHEAU.0000129.

Issa, R.I., 1986. Solution of the implicitly discretised fluid flow equations by operator-splitting. J. Comput. Phys. 62 (1), 40–65. http://dx.doi.org/10.1016/0021-9991(86)90099-9.

Jacobsen, N.G., Fredsoe, J., Jensen, J.H., 2014. Formation and development of a breaker bar under regular waves. Part 1: Model description and hydrodynamics. Coast. Eng. 88, 182–193. http://dx.doi.org/10.1016/j.coastaleng.2013.12.008.

Jacobsen, N.G., Fuhrman, D.R., Fredsøe, J., 2012. A wave generation toolbox for the open-source CFD library: OpenFoam®. Internat. J. Numer. Methods Fluids 70 (9), 1073–1088. http://dx.doi.org/10.1002/fld.2726.

Jin, D., Hoagland, P., Au, D.K., Qiu, J., 2015. Shoreline change, seawalls, and coastal property values. Ocean Coast. Manag. 114, 185–193. http://dx.doi.org/10.1016/j.ocecoaman.2015.06.025.

Kumar, G.M., Sriram, V., 2020. Development of a hybrid model based on mesh and meshfree methods and its application to fluid–elastic structure interaction for free surface waves. J. Fluids Struct. 99, http://dx.doi.org/10.1016/j.jfluidstructs.2020.103159.

Le Méhauté, B., 2013. An Introduction to Hydrodynamics and Water Waves. Springer Science & Business Media.

Li, Y., Ong, M.C., Gudmestad, O.T., Hjertager, B.H., 2020. The effects of slab geometries and wave directions on the steep wave-induced soil response and liquefaction around gravity-based offshore foundations. Ships Offshore Struct. 15 (8), 866–877. http://dx.doi.org/10.1080/17445302.2019.1690736.

Li, Y., Ong, M.C., Tang, T., 2018. Numerical analysis of wave-induced poro-elastic seabed response around a hexagonal gravity-based offshore foundation. Coast. Eng. 136, 81–95. http://dx.doi.org/10.1016/j.coastaleng.2018.02.005.

Liao, K., Hu, C., 2013. A coupled FDM–FEM method for free surface flow interaction with thin elastic plate. J. Mar. Sci. Technol. 18 (1), 1–11. http://dx.doi.org/10.1007/s00773-012-0191-0.

Lin, T.R., Farag, N.H., Pan, J., 2005. Evaluation of frequency dependent rubber mount stiffness and damping by impact test. Appl. Acoust. 66 (7), 829–844. http://dx.doi.org/10.1016/j.apacoust.2004.10.004.

Nicholls, R.J., Cazenave, A., 2010. Sea-level rise and its impact on coastal zones. Science 328 (5985), 1517–1520. http://dx.doi.org/10.1126/science.1185782.

Ning, D., Wang, R., Chen, L., Li, J., Zang, J., Cheng, L., Liu, S., 2017. Extreme wave run-up and pressure on a vertical seawall. Appl. Ocean Res. 67, 188–200. http://dx.doi.org/10.1016/j.apor.2017.07.015.

Peter, M.A., Meylan, M.H., 2010. A general spectral approach to the time-domain evolution of linear water waves impacting on a vertical elastic plate. SIAM J. Appl. Math. 70 (7), 2308–2328. http://dx.doi.org/10.1137/090756557.

Ranasinghe, R., 2016. Assessing climate change impacts on open sandy coasts: A review. Earth-Sci. Rev. 160, 320–332. http://dx.doi.org/10.1016/j.earscirev.2016.07.011.

Reeve, D.E., Soliman, A., Lin, P.Z., 2008. Numerical study of combined overflow and wave overtopping over a smooth impermeable seawall. Coast. Eng. 55 (2), 155–166. http://dx.doi.org/10.1016/j.coastaleng.2007.09.008.

Sree, D.K.K., Mandal, S., Law, A.W.-K., 2021. Surface wave interactions with submerged horizontal viscoelastic sheets. Appl. Ocean Res. 107, http://dx.doi.org/10.1016/j.apor.2020.102483.

Sriram, V., Ma, Q.W., 2012. Improved MLPG_R method for simulating 2D interaction between violent waves and elastic structures. J. Comput. Phys. 231 (22), 7650–7670. http://dx.doi.org/10.1016/j.jcp.2012.07.003.

Toimil, A., Losada, I.J., Nicholls, R.J., Dalrymple, R.A., Stive, M.J.F., 2020. Addressing the challenges of climate change risks and adaptation in coastal areas: A review. Coast. Eng. 156, 103611. http://dx.doi.org/10.1016/j.coastaleng.2019.103611.

Tuković, Ž., Karač, A., Cardiff, P., Jasak, H., Ivanković, A., 2018. OpenFOAM finite volume solver for fluid-solid interaction. Trans. FAMENA 42 (3), 1–31. http://dx.doi.org/10.21278/TOF.42301.

Weller, H.G., Tabor, G., Jasak, H., Fureby, C., 1998. A tensorial approach to computational continuum mechanics using object-oriented techniques. Comput. Phys. 12 (6), http://dx.doi.org/10.1063/1.168744.

Young, W.C., Budynas, R.G., Sadegh, A.M., 2012. Roark's Formulas for Stress and Strain. McGraw-Hill Education.